# Understanding the importance of local magnetic moment in monolayer FeSe

Sudip Pokharel ◉ and Huaxiang Fu ◉

*Department of Physics, University of Arkansas, Fayetteville, Arkansas 72701, USA*

Local magnetic moment (LMM) and antiferromagnetic (AFM) fluctuation play a critical role in affecting the properties of FeSe superconductor. By constraining the local magnetic moment on Fe atoms using density functional theory, we investigate how LMM in FeSe monolayer alters the total energy, heights of Se atoms, band structure, and the electronic properties, for three different AFM spin arrangements which consist of the checkerboard (CB), collinear (CL), and pair-checkerboard (PC) spin phases. We find that (i) the total energy decreases drastically in all three spin structures when LMM develops, showing that the existence of LMM significantly stabilizes the system. The optimal LMM is found to be 2.23, 2.54, and 2.47 $\mu_B$, respectively, in the CB, CL, and PC spin phases. (ii) The heights of Se atoms increase markedly (and in a quadratic manner) with LMM, demonstrating a strong magnetostriction effect. Also intriguingly, we find that the Se heights are insensitive to spin ordering, displaying a rather universal dependence on LMM in three different AFM spin phases. (iii) LMM is shown to alter substantially the electron band structures and Fermi surfaces. Near their optimal LMM, while both CB and PC phases possess electron pockets and no hole pockets, the CL phase exhibits neither electron pockets nor hole pockets, and interestingly, it becomes a semiconductor of a small gap of 60 meV. These results reveal that there is a rich and interesting physics to be tuned by LMM in FeSe superconductor.

## I. INTRODUCTION

Among various iron-based superconductors, FeSe monolayer grown on SrTiO$_3$ substrate attracts much attention due to its unique importance in terms of unveiling the secrets of superconductivity, by possessing a high superconducting-transition temperature ($T_c$) as well as an essentially two-dimensional (2D) structure [1–10]. Bulk FeSe has a transition temperature $T_c$ of 8 K under ambient pressure [11], which increases up to 37 K under pressure [12–14]. However, when grown on SrTiO$_3$ substrate, monolayer FeSe drastically increases $T_c$ to 65 K or even higher [1–3,15], while multilayer FeSe films show no sign of superconductivity [1]. FeSe/SrTiO$_3$ is thus essentially a 2D high-$T_c$ superconductor. Although the exact superconductivity mechanism remains unknown in FeSe/SrTiO$_3$, it is believed to be unconventional and may be of key importance to understand the superconductivity in other iron compounds [16–18]. Furthermore, FeSe is earth abundant and environment friendly, which makes it an excellent material for studying superconductivity.

The precise role of the SrTiO$_3$ substrate in the superconductivity of FeSe/SrTiO$_3$ remains under debate and unsettled. While a phonon replica in the electronic band structure (which is caused by the optic phonon of the substrate) was observed in ARPES experiments [19], theoretical studies revealed that the electron-phonon coupling in FeSe/SrTiO$_3$, although enhanced with respect to in bulk FeSe, cannot explain the observed $T_c$ temperature [20–25] since the electronic screening makes the electron-phonon interaction remain not sufficiently strong [24,25]. It was also previously reported that

the SrTiO$_3$ substrate in FeSe/SrTiO$_3$ does not have a strong chemical-bonding interaction with FeSe [26]. Nevertheless, there is a consensus regarding the functionality of SrTiO$_3$, and the main effects of the substrate are twofolded: one is to provide charge transfer to FeSe [27,28], and the other is to constrain the in-plane lattice constant of the FeSe layer [2,3]. While the exact amount of charge transfer is unsettled, several studies have shown that this transfer is between $-0.06e$ to $-0.12e$ per Fe atom [2,3,29]. The origin of the charge transfer may come from the oxygen vacancies [30,31], adatoms [31], Se vacancies [32], or intrinsically sharing a hole pocket with substrate [33]. The charge transfer may suppress the magnetic ordering and potentially enhance the superconductivity [34], increase the electron density of states at the Fermi surface [35], and/or induce an electric field at interface [29]. Unlike bulk FeSe, FeSe/SrTiO$_3$ shows a distinct Fermi surface. In bulk FeSe, the first Brillouin zone contains both hole pockets around the $\Gamma$ point and electron pockets around the $M$ point [36], while in monolayer FeSe/SrTiO$_3$, there are only electron pockets around the $M$ point [1–3,5,9].

Local magnetic moment (LMM) is related to the unbalanced number of spin-up and spin-down electrons at a given atomic site [i.e., $\int_{\vec{r} \in i} [\rho_\uparrow(\vec{r}) - \rho_\downarrow(\vec{r})] \, d\vec{r}$, where $\rho_\uparrow(\vec{r})$ and $\rho_\downarrow(\vec{r})$ are, respectively, the spin-up and spin-down electron density, and $i$ is the atomic-site index]. LMM is of fundamental importance in altering the material properties, even though the whole solid need not exhibit a net magnetic moment, e.g., in antiferromagnetic (AFM) solids. Specifically, LMM alters the electron charge distributions of different spins around individual atoms, and will profoundly change the

electron-electron interaction (e.g., the exchange interaction) [37], which explains why LMM is important. Furthermore, LMM may critically affect the energetics and the relative stabilities of different structure phases. Moreover, LMM often causes significant change to the topology of Fermi surfaces and hence alters the transport properties such as conductivity and/or superconductivity.

In FeSe, LMM is known to exist at iron sites. For instance, bulk FeSe was shown to exhibit a static magnetic ordering under pressure [38], although the nematic structure transition from the tetragonal to orthorhombic phases at 90 K is not accompanied by a magnetic transition at ambient pressure [39]. Also, antiferromagnetic fluctuation was experimentally revealed in bulk FeSe down to 0 K by nuclear magnetic resonance [40] and inelastic neutron scattering [41]. Furthermore, spin density waves have been detected in a single-layer FeSe/SrTiO$_3$ system [3] and were affected by interface [34]. Magnetic moment and spin density wave were also found theoretically to be stable in bulk FeSe [36]. All signs point to the fact that LMM indeed exists in FeSe. Moreover, by using inelastic neutron scattering, Wang *et al.* found that the scattering of different spins is suppressed upon entering the superconducting state with the opening of a superconducting gap [41]. This reveals that LMM also plays a pivotal role in superconductivity, and studying LMM is thus important.

Despite the importance, LMM in FeSe monolayer is nevertheless not fully understood. More specifically, (i) among various spin structures proposed for FeSe, such as the checkerboard (CB), collinear (CL), and paired checkerboard (PC) phases [26,42,43], it is not clear how LMM changes the energetics of each phase and how the relative stability of different phases may be affected. (ii) It was reported in experiments that the height of Se atoms with respect to the Fe plane is critically linked to superconductivity [44]. It is therefore interesting to study how LMM in FeSe monolayer may alter the Se height. And also intriguingly, how does this modification of Se height by LMM depend on the spin ordering and spin structure? Will this dependence of Se height on LMM differ drastically among the CB, CL, and PC phases? (iii) How does LMM impact the electronic properties such as band structure, Fermi-surface topology, and the density of states (DOS)? Note that these quantities are all closely tied to superconductivity.

There are reasons that the understanding of LMM in FeSe monolayer is limited. First, it is hard to probe in experiments the LMM in single-layer FeSe using neutron scattering since it requires large sample volume. Second, from the theoretical point of view, it is nontrivial to constrain the *local* magnetic moment in individual atoms, particularly in AFM materials where LMM is not uniform. Considering that LMM in FeSe is important, any study on this subject could be very useful.

In this study we perform first-principles spin-polarized density functional calculations to constrain LMM on Fe sites and to investigate their key influences on the energetic, structural, and electronic properties in FeSe monolayer, aimed at obtaining a better understanding of the connection between LMM and superconductivity. We consider FeSe monolayer, instead of FeSe on SrTiO$_3$ substrate, since SrTiO$_3$ is known not to form a strong chemical interaction with FeSe [26]. But we do take into account the charge transfer and the in-plane lattice constraint, which are the two key effects caused by

SrTiO$_3$ substrate [3,27,33]. To account for different possible spin arrangements in the AFM structure of FeSe, we consider three spin structure phases, namely the CB, CL, and PC phases. While we recognize that the spin arrangement in real FeSe/SrTiO$_3$ may be more complicated than these ordered phases by possessing a combination of different motifs of different phases (or by showing a long-range spin fluctuation), considering the spin-ordered structure phases is nevertheless a good and valuable starting point since these ordered phases are the basic motifs in order to form other and more complex spin structures.

We find that, in all three AFM spin structures, the total energy decreases substantially when LMM is allowed, and each phase exhibits an optimal energy at nonzero LMM. Among the three spin structures, the collinear (CL) phase is found to be most stable in monolayer FeSe when the in-plane lattice constant is constrained to the SrTiO$_3$ substrate. This structure stability in monolayer FeSe differs from in bulk FeSe, where the PC phase is most stable. Furthermore, our calculations reveal that the Se height depends drastically on LMM, by increasing quadratically (not linearly) with the magnitude of LMM. Interestingly, we also discover that the dependence of Se height on LMM is nearly identical in all three spin structure phases, showing a universal behavior. This universal behavior further suggests that probing the Se height may provide an important route to monitor the change of LMM in FeSe monolayer. Moreover, we reveal that LMM causes a number of marked changes in the density of states (DOS) and in the electronic band structures. For instance, for each spin phase, the DOS spreads over a wide energy range of 2.5 eV below the Fermi level when LMM is at its optimal value, but is drastically shrunk to a rather narrow energy range of only 1 eV when LMM vanishes. At optimal LMM, both CB and PC phases exhibit only an electron pocket at the Fermi surface, with no appearance of a hole pocket, which is consistent with experiments. Interestingly, the CL phase at its optimal LMM shows neither electron pocket nor hole pocket, and instead it becomes a narrow-gap semimetal. These results show that there is rich, interesting, and insightful physics to learn about the LMM in FeSe monolayer.

## II. THEORETICAL METHODS

Density functional theory (DFT) [45] within the local spin-density approximation (LSDA) [46] is used to determine total energy, atomic forces, and optimal structures, as implemented in QUANTUM ESPRESSO [47]. Norm-conserving pseudopotentials are used [48]. Semicore states of Fe 3$p$ orbitals are treated as the valence states to ensure better accuracy [49]. Our pseudopotentials have been used to determine the spin exchange interaction in FeSe [50] and to study the organic-inorganic hybrid materials [51–54]. The energy cutoff for the plane-wave expansion of the Kohn-Sham single-particle states is 100 Ry, which is tested to be sufficient. Using our pseudopotentials, the optimal lattice constant $a$ and the $c/a$ ratio of bulk FeSe are determined to be $a = 3.67$ Å and $c/a = 1.43$. These results agree with the experimental values of $a = 3.76$ Å and $c/a = 1.46$ [11], as well as with another first-principles result of $a = 3.60$ Å and $c/a = 1.50$ [55].

Based on the facts that the chemical-bonding interaction between FeSe and $SrTiO_3$ substrate is rather weak except that $SrTiO_3$ provides the charge transfer and in-plane lattice-constant constraint [2,3,26–28], we decide to study a single FeSe layer, with a vacuum distance of 10 Å to minimize the interaction between neighboring layers. Meanwhile, we take into account the lattice matching and charge transfer, caused by $SrTiO_3$. The in-plane lattice constant of the FeSe monolayer is constrained to the lattice constant $a = 3.90$ Å of $SrTiO_3$. Furthermore, a charge transfer of $-0.075e$ per Fe atom is included in our calculations. This value of charge transfer is compatible with the value of $-0.085e$ per Fe obtained theoretically [29] and with the value of $-0.089e$ per Fe atom estimated in experiment [2]. Furthermore, by using the electron density $n = 1 \times 10^{14}$ cm$^{-2}$ of 2DEG on $SrTiO_3(001)$ surface [56–58], the charge transfer from $SrTiO_3$ to FeSe is estimated to be $-0.070e$ per Fe atom, which is consistent with our value of charge transfer.

We consider three AFM spin orderings, i.e., the checkerboard (CB), collinear (CL), and pair-checkerboard (PC) magnetic phases. The CB, CL and PC structures along with the spin arrangements on iron atoms are shown respectively in Figs. 1(a)–1(c), where the regions bounded by the solid lines are the magnetic unit cells. For CB phase in Fig. 1(a), each Fe spin is surrounded by four opposite spins, and the unit cell has the same size as the original nonmagnetic unit cell (NMUC), which contains four atoms (two Fe and two Se). For CL phase in Fig. 1(b), each Fe spin is surrounded by two neighboring spins of opposite orientation and two neighboring spins of the same orientation, and the unit cell is $\sqrt{2} \times \sqrt{2}$ of NMUC, which contains eight atoms. For PC phase in Fig. 1(c), each Fe spin is surrounded by three neighboring spins of opposite orientation and one neighboring spin of the same orientation, and the unit cell is $\sqrt{2} \times 2\sqrt{2}$ of NMUC, which contains 16 atoms. The first Brillouin zones in the reciprocal space are depicted in Fig. 1(d) for CB, CL, and PC structures. The atomic positions are optimized for each constrained local magnetic moment in each spin structure. The optimized geometry is subsequently used to determine the energy band structures and the density of states.

Constraint of the local magnetic moments on Fe atoms is performed using the energy penalty functional, and the penalty term enters into the total energy by weight $\lambda$ as $E = E_{\text{LSDA}} + \sum_i \lambda (\mathbf{M}_i - \mathbf{M}_i^0)^2$, where $i$ is the atomic index for Fe atoms and $\mathbf{M}_i^0$ is the targeted LMM at atom $i$. The magnitudes of local magnetic moments at Fe atoms are constrained to a given value $M$, i.e., $|\mathbf{M}_i^0| = M$ for all $i$, while the spin orientations at Fe sites are constrained according to the AFM patterns in Figs. 1(a)–1(c). The magnetic moment need be constrained so that we can determine the possible (metastable) states within the subspace of a given constrained magnetic moment. Without the penalty functional, the energy minimization will be unconstrained, and after relaxation, only the optimal magnetic moment corresponding to the lowest total energy will be yielded (in other words, other metastable states will not be found).

To determine the $\lambda$ value, we consider the CB AFM phase and set the targeted magnitude of LMM on Fe atoms to $M = 0.5$ $\mu_B$. We then choose different $\lambda$ values and determine the real value $M_{\text{real}}$ of LMM at Fe atoms by optimizing the energy
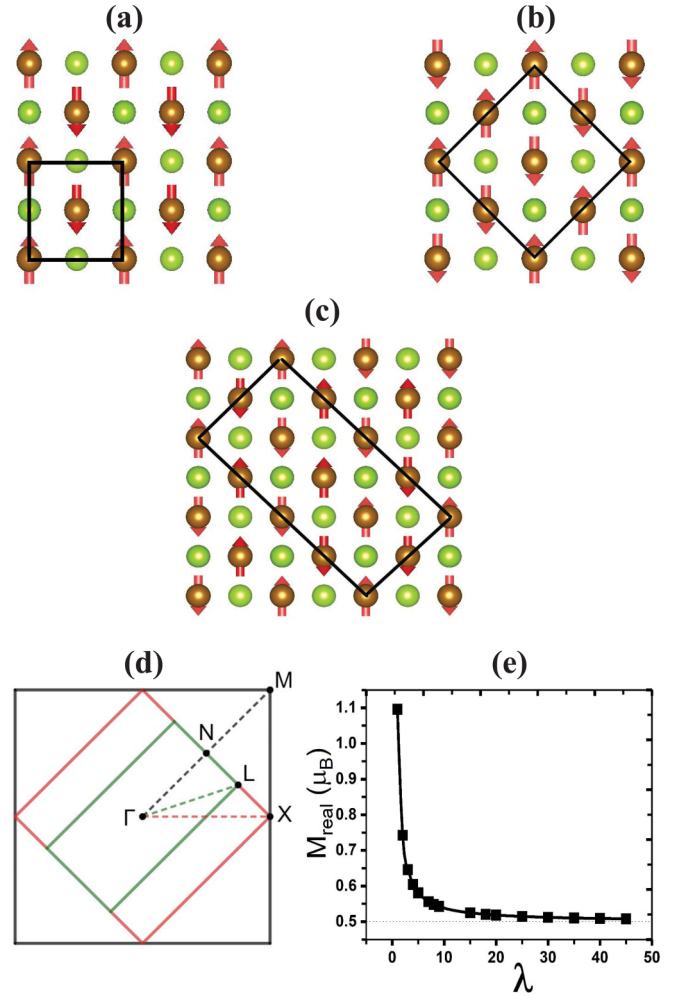


FIG. 1. (a)–(c) Spin arrangements and magnetic unit cells for the CB, CL, and PC phases are shown in (a), (b), and (c), respectively. Fe atoms are shown in brown color with arrows indicating the spin orientation, while Se atoms are shown in green color. The unit cell of each spin structure is depicted by solid lines. (d) The Brillouin zones (BZ) of different spin structures, where the BZs of the CB, CL, and PC structures are the regions bounded by black, red, and green lines, respectively. High-symmetry **k** points such as $\Gamma$, $X$, $M$, $N$, and $L$ are labelled. (e) Local magnetic moment obtained in the constrained-moment calculations as a function of $\lambda$, for the CB phase. For $\lambda = 30$ Ry/$\mu_B^2$ and above, the calculated value ($M_{\text{real}}$) is close to the targeted value of 0.5 $\mu_B$.

$E$. The obtained real magnetic moment $M_{\text{real}}$ as a function of $\lambda$ is shown in Fig. 1(e). Figure 1(e) reveals that, when $\lambda$ increases, the real value $M_{\text{real}}$ of LMM approaches the targeted value, and at $\lambda = 30$ Ry/$\mu_B^2$ or higher, the real value and the targeted value of LMM remain essentially equal. We thus choose $\lambda = 30$ Ry/$\mu_B^2$, and all the subsequent constraints of LMM are performed with this $\lambda$ value.

### III. RESULTS AND DISCUSSIONS

#### A. Energetics of different spin structures

We first investigate how the energies of the three considered spin structures (CB, CL, and PC) are altered by LMM.
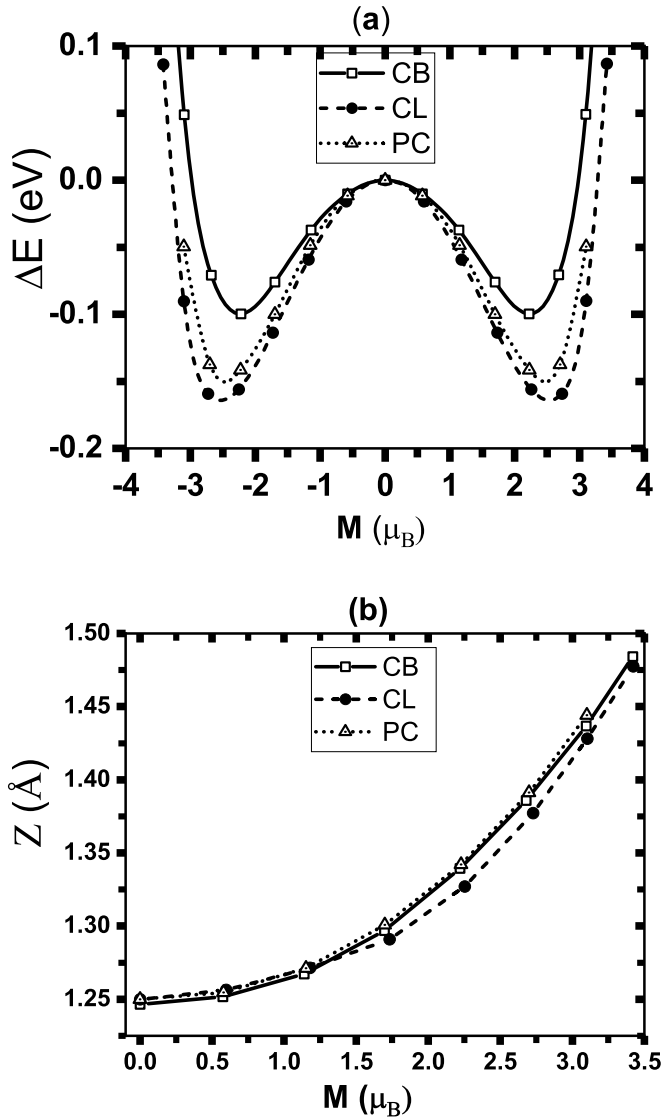
FIG. 2. (a) Energy difference $\Delta E$ per Fe atom as a function of the constrained magnetic moment $M$, for the CB (empty squares), CL (solid dots), and PC (empty triangles) phases. (b) Average height $Z$ of Se atoms as a function of the local magnetic moment $M$.

TABLE I. Optimal local magnetic moment $M_{opt}$ and the minimum energy $\Delta E_{min}$ for each spin structure. The energy difference $\Delta E$ when LMM is constrained at $M = 1.0 \mu_B$ is also given in the fourth column for comparison.

| Phase | $M_{opt}$ ($\mu_B$) | $\Delta E_{min}$ (meV) | $\Delta E$ (meV) |
|-------|--------------------|------------------------|------------------|
| CB    | 2.23               | −100                   | −29              |
| CL    | 2.54               | −164                   | −44              |
| PC    | 2.47               | −151                   | −36              |

For each spin structure, we determine the energy difference $\Delta E \equiv [E(M) - E(M = 0)]/N_{Fe}$, where $E(M)$ is the total energy per unit cell that corresponds to the constrained $M$ value of the local magnetic moment, $E(M = 0)$ is the total energy per unit cell of the nonmagnetic (NM) state (namely we use the energy of the nonmagnetic state as the zero reference), and $N_{Fe}$ is the number of Fe atoms in one unit cell. Note that, by dividing $N_{Fe}$, $\Delta E$ is the energy gain *per Fe atom* due to the existence of LMM, and can thus be directly compared for different spin structures. Figure 2(a) plots $\Delta E$ as a function of local moment $M$. The graph has been symmetrized to the opposite direction of LMM in order to show the double potential wells of local magnetization.

Several outcomes can be made from Fig. 2(a). (i) Our calculations show that LMM does not vanish in all three spin structures. If LMM is to vanish, the NM structure will have the lowest energy, i.e., $\Delta E$ will be positive as LMM becomes nonzero. However, Fig. 2(a) reveals that, for all three phases, $\Delta E$ turns negative as $M$ becomes nonzero, showing that the spin structure with nonvanishing LMM is more stable. (ii) For each spin structure, $\Delta E$ depends sensitively on LMM, or in other words, LMM has a drastic effect on the energetics. More specifically, if we temporarily focus on the CB curve in Fig. 2(a), we see that, as $M$ deviates from zero (i.e., as LMM starts to develop), $\Delta E$ first decreases substantially, and then reaches its minimum $\Delta E_{min} = -100$ meV at an optimal $M_{opt} = 2.23 \mu_B$. Note that $\Delta E_{min} = -100$ meV is much larger in magnitude than the room temperature ($\sim 25$ meV), and thus the CB AFM structure is stable at room temperature. Similar $\Delta E$ behaviors are also found for the CL and PC spin structures, showing a general conclusion that LMM is critically important in all spin structures of single-layer FeSe. (iii) The optimal $M_{opt}$ value of LMM, where $\Delta E$ reaches its minimum, is interestingly similar for three (rather different) spin phases. The optimal $M_{opt}$ and the minimum $\Delta E_{min}$, determined from Fig. 2(a), are given in Table I. Table I shows that $M_{opt}$ is 2.23, 2.54, and 2.47 $\mu_B$, respectively, in the CB, CL, and PC structures, which are all greater than 2.0 $\mu_B$. (iv) Among three spin structures, CL has the deepest well-depth $\Delta E_{min}$ of $-164$ meV (see Table I), which is more stable than PC by 13 meV per Fe atom. Therefore the CL spin structure is most stable in single-layer FeSe. This is different from *bulk* FeSe where the PC structure was reported to be most stable [42]. The difference is not surprising and may be attributed to different in-plane lattice constants; the in-plane lattice is constrained to be 3.90 Å (which matches the SrTiO$_3$ substrate) in our calculations for single-layer FeSe, but is only 3.76 Å in bulk FeSe. The difference also indicates that the effect of the in-plane lattice constraint imposed by SrTiO$_3$ substrate is not negligible.

Our finding of nonzero LMM in FeSe is consistent with, and thus provides a theoretical explanation for, available experimental observations. Although there is no direct experimental measurements of LMM on single-layer FeSe per se, an x-ray emission spectroscopy measurement on FeTe and Fe(Te$_{0.3}$Se$_{0.7}$) reported the existence of local magnetic moment with a magnitude of $\sim 2.0 \mu_B$ [59]. This is in agreement with our calculated values that range from 2.23 to 2.53 $\mu_B$ in different spin phases, although the composition and lattice constant are not exactly the same in theories and experiments. Furthermore, our theories show that LMM does not depend sensitively on the spin ordering and spin arrangement, revealing that the phenomenon of nonzero LMM in monolayer FeSe is generally applicable, largely independent of spin phases.

Our calculations also shed light on possible spin fluctuation in single-layer FeSe. One possible indication of a strong spin fluctuation is measured by whether spins in a local motif can easily change from one spin structure to another. Table I tells us that at optimal $M_{opt}$, $\Delta E_{min}$ of the CL phase and $\Delta E_{min}$ of the PC phase are very close and less than 13 meV, implying that spins may fluctuate strongly between these two phases. On the other hand, at $M_{opt}$, $\Delta E_{min}$ of the CL phase and $\Delta E_{min}$ of the CB phase differ by 64 meV, which is much larger than the thermal energy of room temperature; therefore the thermal energy alone cannot give rise to an effective spin fluctuation between CL and CB.

### B. Heights of Se atoms

Considering that there is experimental evidence which links the heights of Se atoms above the Fe plane to superconductivity [44], it is thus interesting to investigate how LMM at Fe atoms may (or may not) alter the heights of Se atoms. Figure 2(b) depicts the average height of Se atoms, obtained from our constrained-moment DFT structure optimization, as a function of the constrained LMM magnitude $M$ at Fe atoms, for the three considered spin structures. Within each individual spin structure, we find that the heights of different Se atoms are nearly the same, with a deviation of less than $\pm 3\%$. We thus plot in Fig. 2(b) the average height $Z$ of different Se atoms.

Let us first examine the Se height in the CL structure [see the symbols of solid dots in Fig. 2(b)], since CL is the spin structure with the lowest energy. We find that, when the $M$ value increases, the height of Se atoms increases significantly from $Z = 1.250$ Å at $M = 0$ to $Z = 1.430$ Å at $M = 3.12$ $\mu_B$. This large $Z$ change of nearly 0.18 Å is comparable to the ferroelectric atomic off-center displacement of 0.2 Å in BaTiO$_3$ [60], revealing that the heights of Se atoms depend critically on the magnitude of LMM. It also demonstrates that a change in the local magnetic moment of Fe atoms drives a large mechanical position shift of Se atoms (and thus a strong magnetostriction effect in FeSe monolayer), similar to the strong magnetophonon coupling discovered in antiferromagnetic LaFeAsO [61]. One possible origin of this large magnetostriction effect in FeSe monolayer is that, as LMM varies, the spin density around individual Fe atom is changed, which consequently alters the Fe-Se chemical bonding and interaction. Since the heights of Se atoms can be experimentally measured by x-ray diffraction, the correlation between Se height and LMM, found in our calculations, can thus be very useful in estimating the LMM.

Interestingly, if we fix a given magnitude of LMM, say $M = 2.73$ $\mu_B$, and compare the Se heights in *different* spin-structure phases in Fig. 2(b), we find that the Se heights are remarkably similar, being 1.383, 1.377, and 1.387 Å in the CB, CL, and PC phases, respectively. This similarity does not occur by accident. In fact, the Se heights of the three spin structures are close to each other for *all* of the considered LMM values as revealed by our calculations in Fig. 2(b), therefore showing a rather universal phenomenon. It indicates that, while the Se height depends critically on the magnitude of LMM, it nevertheless does not depend on the spin structure and spin ordering. This interesting behavior may be explained by the fact that the Se height is largely determined by the *local* and covalent chemical bonding with neighboring Fe atoms, not by the *global* spin ordering. *For a fixed spin structure*, as LMM varies, the local charge density and the strength of local chemical bonds between Fe and Se atoms are substantially altered, thereby giving rise to a large and sensitive dependence of the Se height on the $M$ value within the given spin structure. On the other hand, when the $M$ value is fixed, different global spin structures (e.g., CB versus CL) do not significantly alter the local chemical bonds, which leads to the insensitivity of the Se height on the spin ordering.

Furthermore, we numerically find that the $M$ dependence of the Se height is well described by an analytical formula $Z = Z_0 + \alpha M^2$ (where $Z_0 = 1.243$ Å is the Se height at $M = 0$), showing that $Z$ depends on $M$ in a quadratic manner. The analytical curves are shown as lines in Fig. 2(b). The coefficient $\alpha$ is determined to be 0.0204, 0.0191, and 0.0202 Å/$\mu_B^2$, respectively, for CB, CL, and PC phases, revealing that $\alpha$ is indeed similar for different spin phases. The analytical formulas should be useful to determine LMM if the Se height is known from experiments or other theories.

### C. Density of states near the Fermi energy

We now study how LMM influences the density of states (DOS), particularly near the Fermi level $E_F$, in each spin structure. Since the origin of superconductivity and pairing mechanism in single-layer FeSe/SrTiO$_3$ remain an unknown mystery yet to be solved, knowledge regarding the electronic properties caused by LMM could help. For each spin structure, we consider three different values of LMM, one at $M = 0$, one near $M = 1.1$ $\mu_B$, and one near $M = 2.2$ $\mu_B$ (which is also close to the optimal LMM value). The calculated DOS is depicted in Figs. 3(a)–3(c) for each spin structure.

Three observations of key relevance can be made from Fig. 3(a), for the CB spin structure. (i) Figure 3(a) reveals that DOS is nonzero at the Fermi level for all three LMM values, showing that the system is metallic. Meanwhile, we notice that there is no sharp DOS peak exactly at the Fermi level $E_F$, suggesting that only a limited number of electron states are available in participating the superconductivity. This small DOS at $E_F$ is similar to the low carrier density found in superconductor LaFeAsO$_{1-x}$F$_x$ [62]. (ii) One rather striking feature in Fig. 3(a) is that, as LMM decreases from 2.22 to 0 $\mu_B$ [from the top curve to the bottom curve in Fig. 3(a)], several peaks of the valence states in the energy region A shift *toward* the Fermi level $E_F$. Meanwhile, one DOS peak in the energy region B slightly moves *away* from $E_F$. As a consequence of these shifts, one giant DOS peak is formed at energy $E \approx -0.5$ eV when the structure becomes NM [see the bottom curve of $M = 0$ in Fig. 3(a)]. (iii) Furthermore, at $M = 0$, DOS largely disappears in region A (i.e., in the energy interval between $-2.6$ to $-1.0$ eV). Combining these results, we thus see that DOS in FeSe monolayer is considerably affected by LMM. We also notice a slight shift for unoccupied conduction states, although this shift is not as pronounced as the valence states. More specifically, as LMM decreases from 2.22 to 0 $\mu_B$ in Fig. 3(a), the DOS peaks of the conduction states in the energy region from 0 to 2 eV visibly shift away from $E_F$.
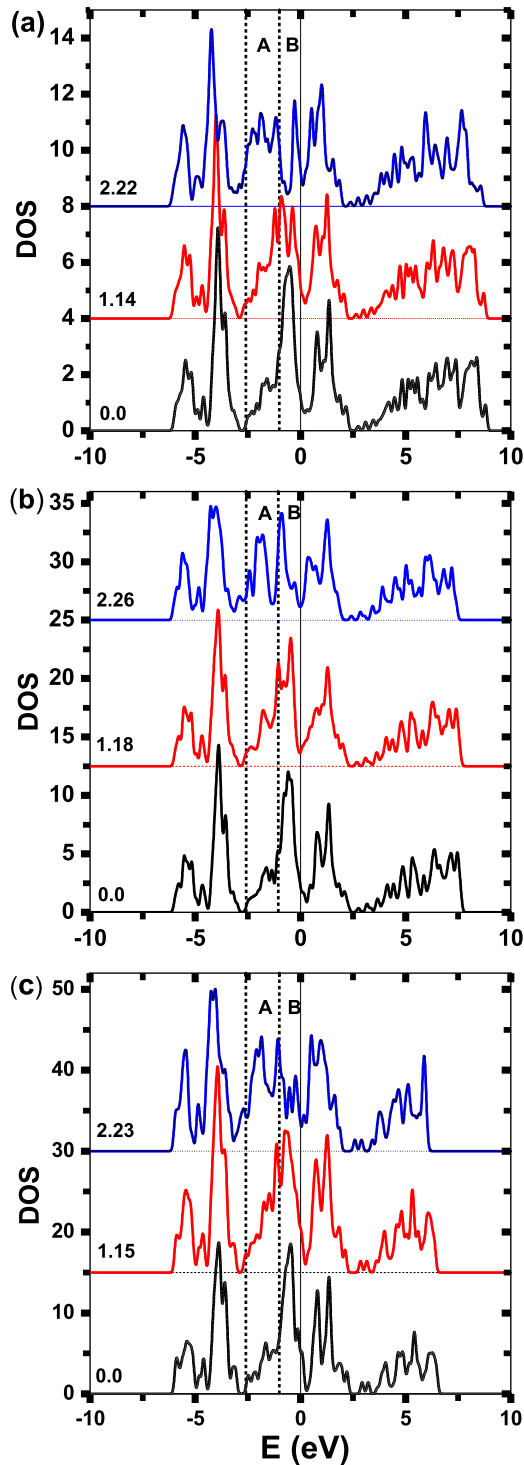
FIG. 3. (a) Density of states (DOS) for the CB spin structure, where LMM is constrained at 0 $\mu_B$ (bottom curve), 1.14 $\mu_B$ (middle curve), and 2.22 $\mu_B$ (top curve). The value of LMM is labeled on an individual curve. (b) DOS for the CL spin structure, where LMM is constrained at 0, 1.18, and 2.26 $\mu_B$, respectively. (c) DOS for the PC spin structure, where LMM is constrained at 0, 1.15, 2.23 $\mu_B$, respectively. The Fermi level is set to be 0 eV in each curve.

Similar conclusions are found true also for DOS in the CL and PC spin structures, which are respectively shown in Figs. 3(b) and 3(c). Specifically, for both CL and PC

structures, when $M$ is high and near 2 $\mu_B$, DOS of valence states spreads from $-2.6$ to 0 eV—and however, when LMM vanishes (i.e., $M = 0$), DOS is narrowed into one strong peak near $-0.5$ eV [63]. In other words, if we focus on the energy region A within the interval $[-2.6, -1.0]$ eV, DOS is high and appears in multiple peaks when $M$ is near 2 $\mu_B$ [see the top curve in Figs. 3(b) and 3(c)], but considerably declines as LMM is reduced to be NM [see the bottom curve in Figs. 3(b) and 3(c)], showing that DOS depends on LMM significantly.

Meanwhile, there are some subtle differences in DOS among different spin phases. For example, we find that, when the LMM value is higher than 2 $\mu_B$, the peak position of DOS in the energy region B is rather different for different spin phases. More specifically, when $M \geqslant 2$ $\mu_B$, the peak in region B is very close to the Fermi level (only $-0.28$ eV below $E_F$) for the CB phase [Fig. 3(a)], and however, for the CL phase in Fig. 3(b), the peak in region B is quite far away from $E_F$ (at $-0.90$ eV below $E_F$). For the PC phase in Fig. 3(c), the peak in region B is weak and barely visible.

Our calculations thus point to that DOS in FeSe monolayer depends sensitively on LMM. Since DOS can be probed by x-ray photoemission spectroscopy (XPS), our finding may provide some useful insight for XPS measurements. If XPS is used to probe the valence states in the energy region $[-2.6, -1.0]$ eV, it may reveal valuable knowledge about LMM in FeSe monolayer. Here it is worth pointing out that the single-particle orbital energies and the bandwidth of the LSDA calculations may not be accurate due to the strong correlation effect. Therefore, the energy ranges of regions A and B may be slightly shifted, and caution need be taken when comparing the theoretical energy region with the experimental one.

### D. Band structures, electron, and hole pockets

Figure 4 shows the electronic band structures for three considered spin structures, and for each spin structure, we consider three different constrained values of LMM. Let us first focus on the band structure of the CB phase in Figs. 4(a)–4(c), where the local Fe moment is constrained to 0, 1.14, and 2.22 $\mu_B$, respectively. (i) For the NM case of $M = 0$, Fig. 4(a) reveals that there are *valence* bands crossing the Fermi level $E_F$ near the zone-center $\Gamma$, and also there are *conduction* bands crossing $E_F$ near the zone-boundary $M$ point. Our calculations thus show that, at the Fermi surface, there are both holelike pockets at $\Gamma$ and electronlike pockets at $M$. (ii) Interestingly, with LMM increasing to 1.14 $\mu_B$ [see Fig. 4(b)], the hole pockets near $\Gamma$ are shrinking considerably, which is caused by the fact that the top two valence bands at $\Gamma$ are shifting downward in energy once LMM becomes nonzero. Meanwhile, the electron pockets at $M$ split into two distinct and well separated sections at $M = 1.14$ $\mu_B$ in Fig. 4(b), showing a substantial difference from the electron pockets in Fig. 4(a). (iii) As LMM is further increased to $M = 2.22$ $\mu_B$ [Fig. 4(c)], the hole pockets at $\Gamma$ disappear since the top valence bands submerge below the Fermi level, and only the electron pockets at $M$ remain. (iv) Also notably, if we examine the sizes of the electron pockets at $M$, we see that, when LMM varies from 0 in Fig. 4(a) to 2.22 $\mu_B$ in Fig. 4(c), the size of the *upper* electron pocket decreases, while the size of the *lower* electron pocket increases. Our calculations
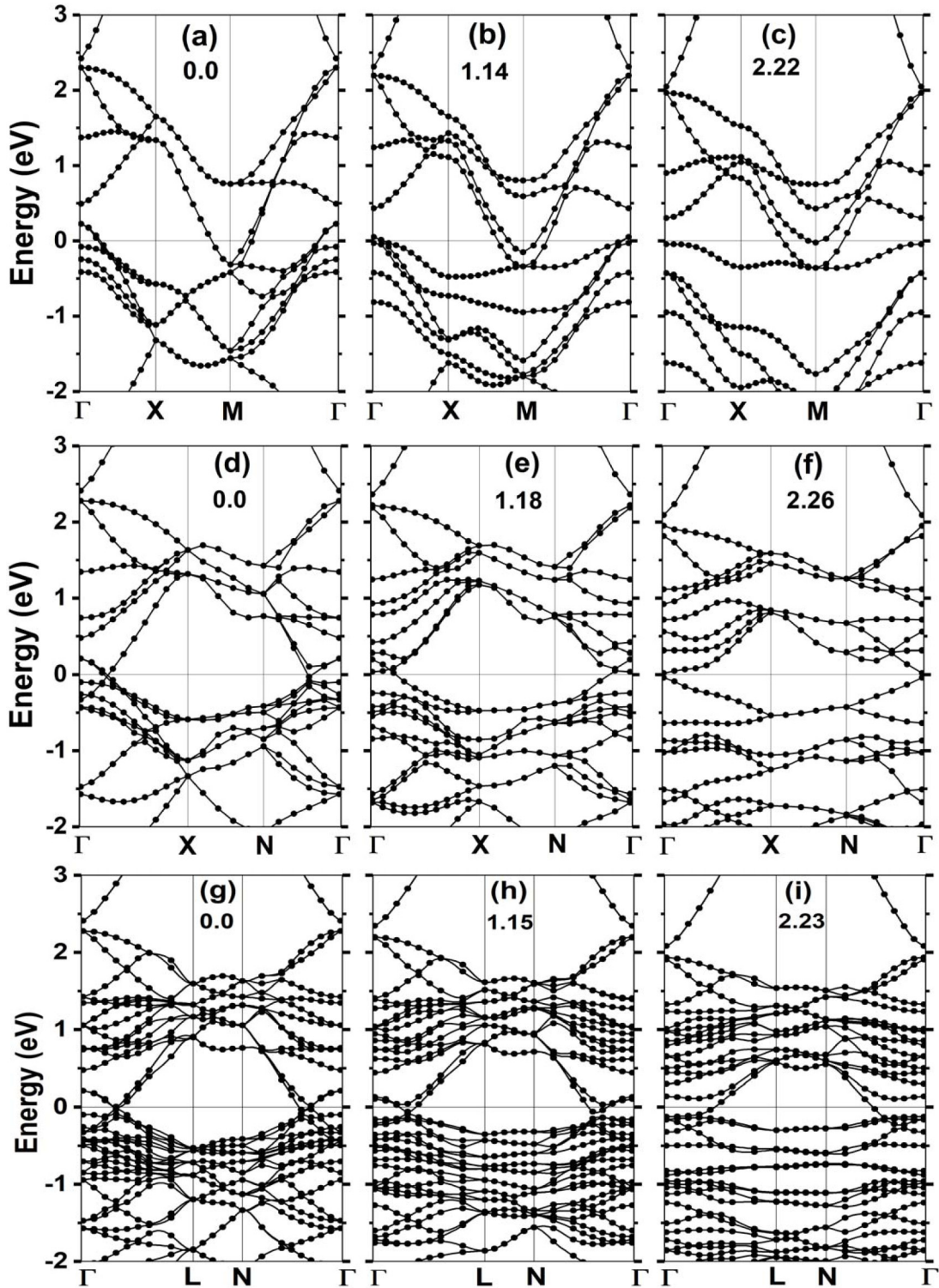
FIG. 4. Electronic band structures for the following spin structures: CB [upper panel (a)–(c)], CL [middle panel (d)–(f)], and PC [lower panel (g)–(i)]. For each spin phase, band structures at three different LMMs, with their values labeled in each figure [e.g., 0, 1.14, 2.22 $\mu_B$, respectively, in (a)–(c) for the CB phase], are studied. The Fermi level $E_F$ is set to be 0 eV in each figure. The Brillouin zone and the high-symmetry **k** points are given in Fig. 1(d) for the three considered spin structures.

thus reveal that the electron band structure and the Fermi pockets are very sensitive to LMM. For this reason, LMM may therefore serve as an effective physical quantity to tune the electronic bands as well as the Fermi topology in FeSe superconductors.

Other important observations can also be made from Figs. 4(a)–4(c). Looking at the *valence* bands at the zone center $\Gamma$ in Fig. 4(a) (i.e., $M = 0$), we find that the energies of different valence bands are very close to each other, and in fact, at the zone center $\Gamma$, the energies are mostly located in

a rather narrow energy range from $-0.5$ to $0.25$ eV. As LMM increases to $M = 1.14$ $\mu_B$ [Fig. 4(b)], the energy separation among valence bands at $\Gamma$ is significantly enlarged, and finally at $M = 2.2$ $\mu_B$ [Fig. 4(c)], the valence bands at $\Gamma$ become well separated. This reveals that LMM drastically affects *multiple* bands, not just the band at the Fermi level. Our calculations also imply that probing the multibands structure in experiments may reveal more and important insight into LMM, which could provide a key connection with superconductivity. Furthermore, as multiple valence bands are well separated at $M = 2.22$ $\mu_B$, we find that the band dispersion of the top valence band becomes rather flat between $-0.5$ and $0$ eV in Fig. 4(c), which explains why a sharp DOS peak forms in the energy region B at this LMM value [see the top curve in Fig. 3(a)]. The formation of the flat band at $M = 2.22$ $\mu_B$ can be attributed to the multiband interaction, namely when other valence bands shift down in energy due to the increase of LMM, they push upwards the top valence band and make it to be well separated from the rest of valence bands, which gives rise to a flat band dispersion.

Compared to the CB spin phase, the band structures of the CL spin phase are interestingly different [see Figs. 4(d)–4(f) in the middle panel]. At $M = 0$ there are both electron and hole pockets at the zone center $\Gamma$ [Fig. 4(d)]. Note that the $M$ point (and thus the electron pocket) in the Brillouin zone of the CB phase is folded to the $\Gamma$ point in the CL phase as shown in Fig. 1(d), since CL is a magnetic supercell. As LMM increases to $1.18$ $\mu_B$ [Fig. 4(e)], the electron pocket at $\Gamma$ disappears in CL, while the hole pocket remains. The disappearance of the electron pocket in CL is rather unusual, since it does not occur in other spin structures. More intriguingly, when $M$ is further increased to $2.26$ $\mu_B$, no bands are found to cross the Fermi level, and the system becomes a semiconductor (or semimetal) with a direct band gap of $60$ meV [Fig. 4(f)]. In other words, both electron and hole pockets disappear near the optimal LMM value in the CL phase, which differs drastically from what occurs in the CB phase.

For the band structures of the PC spin phase in Figs. 4(g)–4(i), we see that the NM structure at $M = 0$ exhibits both electron and hole pockets at $\Gamma$ [Fig. 4(g)], similar to the CL phase. When the LMM value is increased to $1.15$ $\mu_B$ in Fig. 4(h), the hole pocket at $\Gamma$ shrinks due to the fact that the top valence band shifts downward in energy. As $M$ is further increased to $2.23$ $\mu_B$ in Fig. 4(i), the hole pocket completely disappears, leaving only an electron pocket at $\Gamma$. We thus see that, when the PC spin phase is near its optimal LMM value, there is only electron pocket remaining, with no hole pocket occurring at the Fermi surface.

Contrasting the band structures of three spin phases, we recognize some similarities which are common to all phases: (i) There are both electron and hole pockets at the Fermi surface for the nonmagnetic case, and (ii) the hole pockets are pushed downward as LMM increases, and finally disappear when $M$ is close to the optimal value of each individual spin phase. Nevertheless, the band structures of the three spin phases also show interesting differences, particularly at high LMM. As LMM is higher than $2$ $\mu_B$, while the CB and PC phases exhibit electron pockets at the Fermi level, CL does not. Also, there is a subtle difference in the electron pocket between the CB and PC phases when LMM is larger than

$2$ $\mu_B$. In the CB phase, there are two electron pockets in Fig. 4(c), one with a large size and one with a small size. But in the PC phase, there is only one electron pocket in Fig. 4(i).

We further perform calculations to unfold the band structures of the CL and PC phases [64], since the real-space unit cells of both phases are a superstructure with respect to the CB phase. The unfolded band structures are given in Fig. 5 for the CL and PC phases (no band unfolding is needed for the CB phase). We see from Fig. 5 that, near the optimal local magnetic moment, the CL phase is a small-gap insulator [Fig. 5(c)], and the PC phase possesses an electron pocket at $M$ point and no hole pocket at $\Gamma$ point [Fig. 5(f)]. The unfolded band structures thus further confirm that both the PC phase and the CB phase yield a theoretical band structure which is consistent with the experimental measurement, while the CL phase does not.

Our theoretical band structures provide valuable implication and useful insight into the superconductivity in FeSe/SrTiO$_3$. By using ARPES technique, it was reported in experiments that there are only electronlike pockets at $E_F$, with no observation of holelike pockets, in single-layer FeSe/SrTiO$_3$ [2,3,9]. Assume that LMM is fluctuating near its optimal value, which is reasonable since the local magnetic moment about $2.0$ $\mu_B$ was indeed observed experimentally in Fe(SeTe) [59]. Then, according to our calculation results in Figs. 4(c) and 4(i), it is likely that the superconducting phase in FeSe/SrTiO$_3$ originates from the motifs with CB or PC spin structure [65], since these structures yield a band structure with only electron pocket, consistent with the experiments. In contrast, the CL spin structure with stripe ordering is less likely to contribute to the superconductivity, for this structure is an insulator without electron pockets.

## IV. CONCLUSIONS

By performing density-functional calculations with constrained local magnetic moments for monolayer FeSe in different spin phases, we have conducted a rather comprehensive study on how the LMM value may influence the energetics, the Se height, the density of states, and the electronic band structures. Our main findings are summarized in the following.

(i) When LMM becomes nonzero, the energies of the three spin phases are found to decrease drastically, and as a consequence, LMM does not vanish in all three phases. The optimal LMM value (at which the energy is at minimum) is determined to be $2.23$, $2.54$, and $2.47$ $\mu_B$ for the CB, CL, and PC phases, respectively. These theoretical LMM values agree well with the experimental value of $\sim 2.0$ $\mu_B$ [59]. The optimal energy gain between the magnetic and nonmagnetic structures is determined to be $-100$, $-164$, and $-151$ meV per Fe atom, respectively, for the CB, CL, and PC phases. These energy gains are much larger than the thermal energy at room temperature, revealing that each AFM structure is more stable than the nonmagnetic phase. Also, in monolayer FeSe with lattice constant constrained to SrTiO$_3$, we find that the CL phase is the most stable spin structure, which differs from the FeSe bulk where the PC phase is most stable [42].
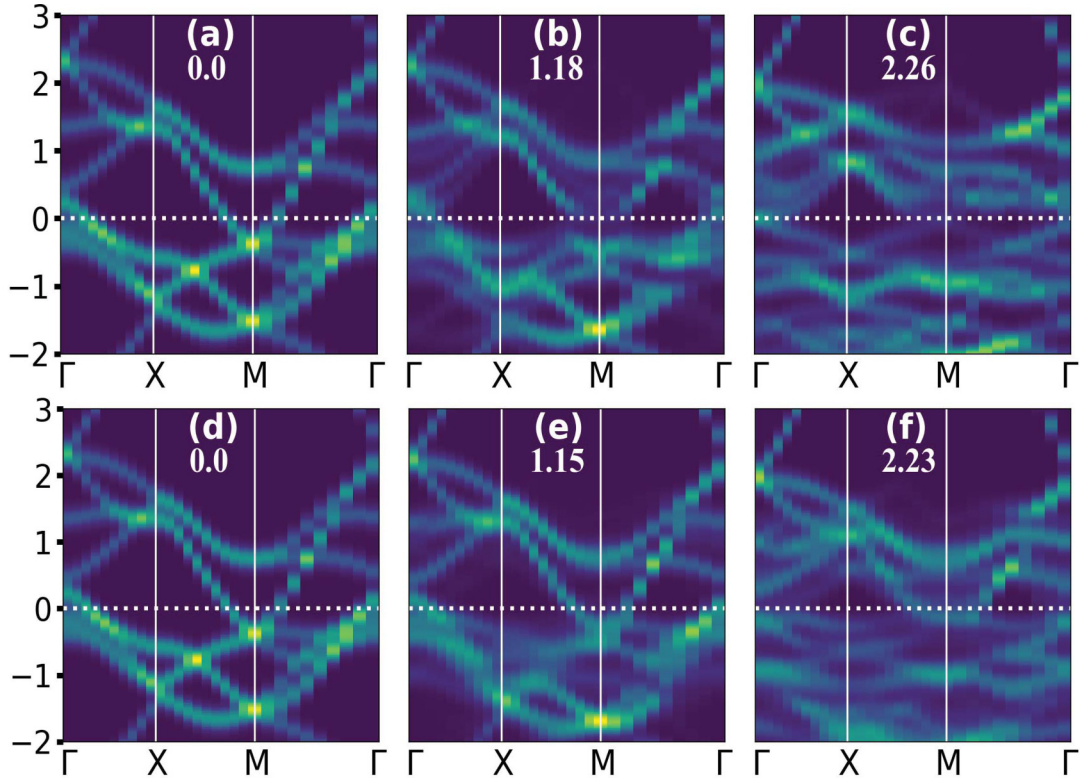
FIG. 5. Unfolded band structures for the following spin phases: CL [upper panel (a)–(c)], and PC [lower panel (d)–(f)]. No band unfolding is needed for the CB phase. The vertical axis is the Kohn-Sham single-particle energies (in eV), and the horizontal axis is the high-symmetry **k** points of the unfolded Brillouin zone of the CB phase. For each spin phase, band structures at three different LMMs, with their values labeled in each figure [e.g., 0, 1.18, 2.26 $\mu_B$, respectively, in (a)–(c) for the CL phase], are studied. The Fermi level $E_F$ is set to be 0 eV in each figure.

(ii) The Se height is revealed to depend sensitively on LMM. As LMM increases, the Se height is found to increase drastically and in a quadratic manner, showing a strong magnetostriction effect. More intriguingly, we discover that the correlation between the Se height and the LMM value is remarkably similar for three different spin phases, revealing a rather universal phenomenon. This universal behavior demonstrates that the Se height depends largely on the local Fe-Se chemical bonding rather than the global spin ordering. Since the Se height can be measured by x-ray diffraction, the quantitative relationship which we found between the Se height and LMM may thus be an effective route to determine the (important) LMM in monolayer FeSe.

(iii) Furthermore, LMM is critical in affecting the densities of states. We find that the energy region where DOS can be dramatically altered by LMM is between $-2.6$ and $-1.0$ eV below the Fermi level. When LMM is large and near 2 $\mu_B$, there are several sharp DOS peaks that spread in the above energy region. However, when LMM vanishes, DOS in this energy region largely disappears since the electron states are found to shift toward the Fermi level. This finding reveals that probing DOS in experiments, particularly in the specific energy region as given above, may uncover the important information between superconductivity and LMM.

(iv) Our calculations further show that LMM plays a pivotal role in altering the electronic band structure and Fermi surface. For a nonmagnetic structure with a vanishing (or nearly vanishing) LMM, each spin phase is found to possess both electron pockets and hole pockets. However, as LMM develops, different spin phases exhibit rather different evolutions in terms of band structure and Fermi topology. At large LMM values when $M \geqslant 2\ \mu_B$, the CB phase is found to possess two electron pockets and no hole pocket; the CL phase possesses neither electron pocket nor hole pockets, and interestingly the system becomes a small-gap semiconductor with a band gap of 60 meV; the PC phase possesses one electron pocket and no hole pocket.

These results reveal that there is rich and interesting physics regarding the LMM in FeSe monolayer. We wish our study will stimulate more theoretical and experimental interest in this important subject.

[1] D. Liu, W. Zhang, D. Mou, J. He, Y. B. Ou, Q. Y. Wang, Z. Li, L. Wang, L. Zhao, S. He, Y. Peng, X. Liu, C. Chen, L. Yu, G. Liu, X. Dong, J. Zhang, C. Chen, Z. Xu, J. Hu *et al.*, Nat. Commun. **3**, 931 (2012).

[2] S. He, J. He, W. Zhang, L. Zhao, D. Liu, X. Liu, D. Mou, Y. B. Ou, Q. Y. Wang, Z. Li, L. Wang, Y. Peng, Y. Liu, C. Chen, L. Yu, G. Liu, X. Dong, J. Zhang, C. Chen, Z. Xu *et al.*, Nat. Mater. **12**, 605 (2013).

[3] S. Tan, Y. Zhang, M. Xia, Z. Ye, F. Chen, X. Xie, R. Peng, D. Xu, Q. Fan, H. Xu, J. Jiang, T. Zhang, X. Lai, T. Xiang, J. Hu, B. Xie, and D. Feng, Nat. Mater. **12**, 634 (2013).

[4] Y. Sun, W. Zhang, Y. Xing, F. Li, Y. Zhao, Z. Xia, L. Wang, X. Ma, Q.-K. Xue, and J. Wang, Sci. Rep. **4**, 6040 (2014).

[5] X. Liu, L. Zhao, S. He, J. He, D. Liu, D. Mou, B. Shen, Y. Hu, J. Huang, and X. J. Zhou, J. Phys.: Condens. Matter **27**, 183201 (2015).

[6] R. Peng, X. P. Shen, X. Xie, H. C. Xu, S. Y. Tan, M. Xia, T. Zhang, H. Y. Cao, X. G. Gong, J. P. Hu, B. P. Xie, and D. L. Feng, Phys. Rev. Lett. **112**, 107001 (2014).

[7] R. Peng, H. C. Xu, S. Y. Tan, H. Y. Cao, M. Xia, X. P. Shen, Z. C. Huang, C. H. P. Wen, Q. Song, T. Zhang, B. P. Xie, X. G. Gong, and D. L. Feng, Nat. Commun **5**, 5044 (2014).

[8] Q. Fan, W. H. Zhang, X. Liu, Y. J. Yan, M. Q. Ren, R. Peng, H. C. Xu, B. P. Xie, J. P. Hu, T. Zhang, and D. L. Feng, Nat. Phys. **11**, 946 (2015).

[9] D. Liu, C. Li, J. Huang, B. Lei, L. Wang, X. Wu, B. Shen, Q. Gao, Y. Zhang, X. Liu, Y. Hu, Y. Xu, A. Liang, J. Liu, P. Ai, L. Zhao, S. He, L. Yu, G. Liu, Y. Mao *et al.*, Phys. Rev. X **8**, 031033 (2018).

[10] D. Huang, C.-L. Song, T. A. Webb, S. Fang, C.-Z. Chang, J. S. Moodera, E. Kaxiras, and J. E. Hoffman, Phys. Rev. Lett. **115**, 017002 (2015).

[11] F. C. Hsu, J. Y. Luo, K. W. Yeh, T. K. Chen, T. W. Huang, P. M. Wu, Y. C. Lee, Y. L. Huang, Y. Y. Chu, D. C. Yan, and M. K. Wu, Proc. Natl. Acad. Sci. **105**, 14262 (2008).

[12] S. Medvedev, T. M. McQueen, I. A. Troyan, T. Palasyuk, M. I. Eremets, R. J. Cava, S. Naghavi, F. Casper, V. Ksenofontov, G. Wortmann, and C. Felser, Nat. Mater. **8**, 630 (2009).

[13] Y. Mizuguchi, Y. Hara, K. Deguchi, S. Tsuda, T. Yamaguchi, K. Takeda, H. Kotegawa, H. Tou, and Y. Takano, Supercond. Sci. Technol. **23**, 054013 (2010).

[14] S. Margadonna, Y. Takabayashi, Y. Ohishi, Y. Mizuguchi, Y. Takano, T. Kagayama, T. Nakagawa, M. Takata, and K. Prassides, Phys. Rev. B **80**, 064506 (2009).

[15] J.-F. Ge, Z.-L. Liu, C. Liu, C.-L. Gao, D. Qian, Q.-K. Xue, Y. Liu, and J.-F. Jia, Nat. Mater. **14**, 285 (2015).

[16] F. Wang and D.-H. Lee, Science **332**, 200 (2011).

[17] J. K. Glasbrenner, I. I. Mazin, H. O. Jeschke, P. J. Hirschfeld, R. M. Fernandes, and R. Valenti, Nat. Phys. **11**, 953 (2015).

[18] D.-H. Lee, Chin. Phys. B **24**, 117405 (2015).

[19] J. J. Lee, F. T. Schmitt, R. G. Moore, S. Johnston, Y.-T. Cui, W. Li, M. Yi, Z. K. Liu, M. Hashimoto, Y. Zhang, D. H. Lu, T. P. Devereaux, D.-H. Lee, and Z.-X. Shen, Nature (London) **515**, 245 (2014).

[20] B. Li, Z. W. Xing, G. Q. Huang, and D. Y. Xing, J. Appl. Phys. **115**, 193907 (2014).

[21] T. Bazhirov and M. L. Cohen, Phys. Rev. B **86**, 134517 (2012).

[22] L. Rademaker, Y. Wang, T. Berlijn, and S. Johnston, New J. Phys. **18**, 022001 (2016).

[23] X. Xu, S. Zhang, X. Zhu, and J. Guo, J. Phys.: Condens. Matter **32**, 343003 (2020).

[24] L. P. Gor'kov, Phys. Rev. B **93**, 060507(R) (2016).

[25] Y. Zhou and A. J. Millis, Phys. Rev. B **96**, 054516 (2017).

[26] K. Liu, Z. Y. Lu, and T. Xiang, Phys. Rev. B **85**, 235123 (2012).

[27] H. Zhang, D. Zhang, X. Lu, C. Liu, G. Zhou, X. Ma, L. Wang, P. Jiang, Q.-K. Xue, and X. Bao, Nat. Commun. **8**, 214 (2017).

[28] W. Zhang, Z. Li, F. Li, H. Zhang, J. Peng, C. Tang, Q. Wang, K. He, X. Chen, L. Wang, X. Ma, and Q.-K. Xue, Phys. Rev. B **89**, 060506(R) (2014).

[29] F. Zheng, Z. Wang, W. Kang, and P. Zhang, Sci. Rep. **3**, 2213 (2013).

[30] J. Bang, Z. Li, Y. Y. Sun, A. Samanta, Y. Y. Zhang, W. Zhang, L. Wang, X. Chen, X. Ma, Q.-K. Xue, and S. B. Zhang, Phys. Rev. B **87**, 220503(R) (2013).

[31] K. V. Shanavas and D. J. Singh, Phys. Rev. B **92**, 035144 (2015).

[32] T. Berlijn, H.-P. Cheng, P. J. Hirschfeld, and W. Ku, Phys. Rev. B **89**, 020501(R) (2014).

[33] Y. N. Huang and W. E. Pickett, Phys. Rev. B **95**, 165107 (2017).

[34] H.-Y. Cao, S. Tan, H. Xiang, D. L. Feng, and X.-G. Gong, Phys. Rev. B **89**, 014501 (2014).

[35] T. Bazhirov and M. L. Cohen, J. Phys.: Condens. Matter. **25**, 105506 (2013).

[36] A. Subedi, L. Zhang, D. J. Singh, and M. H. Du, Phys. Rev. B **78**, 134514 (2008).

[37] S. Coh, M. L. Cohen, and S. G. Louie, New J. Phys. **17**, 073027 (2015).

[38] M. Bendele, A. Amato, K. Conder, M. Elender, H. Keller, H.-H. Klauss, H. Luetkens, E. Pomjakushina, A. Raselli, and R. Khasanov, Phys. Rev. Lett. **104**, 087003 (2010).

[39] T. M. McQueen, A. J. Williams, P. W. Stephens, J. Tao, Y. Zhu, V. Ksenofontov, F. Casper, C. Felser, and R. J. Cava, Phys. Rev. Lett. **103**, 057002 (2009).

[40] T. Imai, K. Ahilan, F. L. Ning, T. M. McQueen, and R. J. Cava, Phys. Rev. Lett. **102**, 177005 (2009).

[41] Q. Wang, Y. Shen, B. Pan, X. Zhang, K. Ikeuchi, K. Iida, A. D. Christianson, H. C. Walker, D. T. Adroja, M. Abdel-Hafiez, X. Chen, D. A. Chareev, A. N. Vasiliev, and J. Zhao, Nat. Commun. **7**, 12182 (2016).

[42] H.-Y. Cao, S. Chen, H. Xiang, and X.-G. Gong, Phys. Rev. B **91**, 020504(R) (2015).

[43] K. Liu, B.-J. Zhang, and Z.-Y. Lu, Phys. Rev. B **91**, 045107 (2015).

[44] C.-L. Song, Y.-L. Wang, Y.-P. Jiang, Z. Li, L. Wang, K. He, X. Chen, J. E. Hoffman, X.-C. Ma, and Q.-K. Xue, Phys. Rev. Lett. **112**, 057002 (2014).

[45] P. Hohenberg and W. Kohn, Phys. Rev. **136**, B864 (1964).

[46] S. H. Vosko, L. Wilk, and M. Nusair, Can. J. Phys **58**, 1200 (1980).

[47] P. Giannozzi, S. Baroni, N. Bonini, M. Calandra, R. Car, C. Cavazzoni, D. Ceresoli, G. L. Chiarotti, M. Cococcioni, I. Dabo, A. D. Corso, S. de Gironcoli, S. Fabris, G. Fratesi, R. Gebauer, U. Gerstmann, C. Gougoussis, A. Kokalj, M. Lazzeri, L. Martin-Samos *et al.*, J. Phys: Condens. Matter **21**, 395502 (2009).

[48] N. Troullier and J. L. Martins, Phys. Rev. B **43**, 1993 (1991).

[49] The configuration for generating pseudopotentials is $3p^6 3d^6 4s^1$ for Fe and $4s^2 4p^{3.5} 4d^{0.1}$ for Se. The matching radii of pseudowave function and all-electron wave function are $r_{cut}^{s,p,d} =$ 1.90, 1.70, 1.70 bohrs for Fe, and $r_{cut}^{s,p,d} =$ 1.80, 1.80, 2.30 bohrs for Se. The screened Coulomb potential with $r_c = 1.90$ bohrs is used as the local channel for Fe, and the $4p$ pseudopotential is used as the local channel for Se.

[50] S. Pokharel and H. Fu (unpublished).

[51] A. Nazzal and H. Fu, Phys. Rev. B **72**, 075202 (2005).

[52] H. Fu and J. Li, J. Chem. Phys. **120**, 6721 (2004).

[53] X. Huang, J. Li, and H. Fu, J. Am. Chem. Soc. **122**, 8789 (2000).

[54] Y. Zhang, Z. Islam, Y. Ren, P. A. Parilla, S. P. Ahrenkiel, P. L. Lee, A. Mascarenhas, M. J. McNevin, I. Naumov, H.-X. Fu, X.-Y. Huang, and J. Li, Phys. Rev. Lett. **99**, 215901 (2007).

[55] A. P. Koufos, D. A. Papaconstantopoulos, and M. J. Mehl, Phys. Rev. B **89**, 035150 (2014).

[56] A. F. Santander-Syro, O. Copie, T. Kondo, F. Fortuna, S. Pailhès, R. Weht, X. G. Qiu, F. Bertran, A. Nicolaou, A. Taleb-Ibrahimi, P. Le Fèvre, G. Herranz, M. Bibes, N. Reyren, Y. Apertet, P. Lecoeur, A. Barthèlèmy, and M. J. Rozenberg, Nature (London) **469**, 189 (2011).

[57] W. Meevasana, P. D. C. King, R. H. He, S.-K. Mo, M. Hashimoto, A. Tamai, P. Songsiriritthigul, F. Baumberger, and Z.-X. Shen, Nat. Mater. **10**, 114 (2011).

[58] W. Zhao, M. Li, C.-Z. Chang, J. Jiang, L. Wu, C. Liu, J. S. Moodera, Y. Zhu, and M. H. W. Chan, Sci. Adv. **4**, eaao2682 (2018).

[59] H. Gretarsson, A. Lupascu, J. Kim, D. Casa, T. Gog, W. Wu, S. R. Julian, Z. J. Xu, J. S. Wen, G. D. Gu, R. H. Yuan, Z. G. Chen, N.-L. Wang, S. Khim, K. H. Kim, M. Ishikado, I. Jarrige, S. Shamoto, J.-H. Chu, I. R. Fisher, and Y.-J. Kim, Phys. Rev. B **84**, 100509(R) (2011).

[60] H. Fu and R. E. Cohen, Nature (London) **403**, 281 (2000).

[61] Z. P. Yin, S. Lebegue, M. J. Han, B. P. Neal, S. Y. Savrasov, and W. E. Pickett, Phys. Rev. Lett. **101**, 047001 (2008).

[62] D. J. Singh and M.-H. Du, Phys. Rev. Lett. **100**, 237003 (2008).

[63] The DOSs for nonmagnetic systems in three spin structures are similar as they should be. The slight difference is caused by the different **k**-point samplings for different spin structures.

[64] V. Popescu and A. Zunger, Phys. Rev. B **85**, 085201 (2012).

[65] Since, at the optimal LMM, the energy of the PC phase ($-151$ meV per Fe atom) is substantially lower than that of the CB phase ($-100$ meV per Fe atom), the PC spin phase is more stable and may be more likely to be responsible for the superconductivity in $FeSe/SrTiO_3$.